

Toward an Understanding of the Growth of Ag Filaments on α - Ag_2WO_4 and Their Photoluminescent Properties: A Combined Experimental and Theoretical Study

Elson Longo,[†] Diogo P. Volanti,^{*,‡} Valéria M. Longo,[†] Lourdes Gracia,[§] Içamira C. Nogueira,[⊥] Marcio A. P. Almeida,[†] Antonio N. Pinheiro,[⊥] Mateus M. Ferrer,[⊥] Laécio S. Cavalcante,^{||} and Juan Andrés[§]

[†]Instituto de Química, UNESP—Universidade Estadual Paulista, R. Francisco Degni, 55, Araraquara 14800-900, Brazil

[‡]Departamento de Química e Ciências Ambientais, UNESP—Universidade Estadual Paulista, R. Cristóvão Colombo, 2265, São José do Rio Preto 15054-000, Brazil

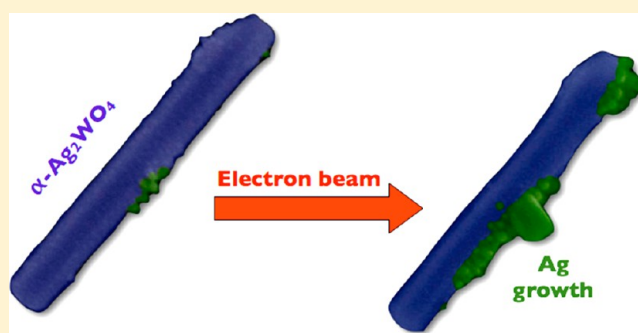
[§]Departament de Química Física i Analítica, UJI—Universitat Jaume I, Av. de Vicent Sos Baynat, s/n, Castelló de la Plana 12071, Spain

[⊥]Departamento de Química, UFSCar—Universidade Federal de São Carlos, Rod. Washington Luis, km 235, São Carlos 13565-905, Brazil

^{||}Departamento de Química, UESPI—Universidade Estadual do Piauí, R. João Cabral, 2231, Teresina 64002-150, Brazil

S Supporting Information

ABSTRACT: A combined experimental and theoretical study was conducted on the structure and electronic properties of α - Ag_2WO_4 to clarify the nucleation and growth processes of Ag filaments on α - Ag_2WO_4 crystals induced by electron beam irradiation under electron microscopy. X-ray diffraction with Rietveld analysis, micro-Raman and Fourier-transform infrared spectroscopy were used to analyze the structural order/disorder of α - Ag_2WO_4 crystals. These complementary techniques indicated that the microwave-assisted hydrothermal method employed in the synthesis of α - Ag_2WO_4 crystals leads to the freezing of distorted $[\text{WO}_6]$ and $[\text{AgO}_y]$ ($y = 2, 4, 6$ and 7) clusters as the constituent polyhedra of α - Ag_2WO_4 . On the basis of the theoretical and experimental results, we provide a complete assignment of the structure of α - Ag_2WO_4 and describe the relationship among the disorder, nucleation growth, rate of Ag formation, and photoluminescence behavior before and after the irradiation of the accelerated electron beam. Density functional theory (DFT) studies indicated significant changes in the order–disorder of the initial α - Ag_2WO_4 electronic structure, with a decrease in the band gap value from 3.55 to 2.72 eV. The first stages of the electron irradiation on α - Ag_2WO_4 crystal were investigated by DFT calculations, and we have derived a mechanism to describe the formation and growth of Ag filaments during the electronic excitation of the $[\text{AgO}_2]$ cluster.



1. INTRODUCTION

Nanoparticle growth mechanisms have received much attention in recent years; controlling the size and morphologies of nanostructures is important for technological application. In this context, *in situ* electron microscopy constitutes an elegant technique that uncovers dynamic processes in the growth of nanocrystals. Recent technological advancements, in conjunction with high-resolution imaging, provide a new opportunity to view nanoscale processes. These advancements have been made possible as a result of the expansion and diffusion of transmission electron microscopy (TEM) heating holders for *in situ* electron microscopy.^{1–5} Several studies have reported using the TEM heating holder to monitor the crystal growth of different nanomaterials, such as bismuth,⁶ germanium,⁷ indium–arsenide,⁸ and vanadium oxide,⁹ and *in situ* liquid

TEM has been employed to understand the growth process of copper and lead sulfide nanostructures.^{10–12} The greatest impact of this new method of investigating the stages of crystal growth is the possibility to observe the step-by-step evolution of the crystal at the nanoscale.^{13,14}

The preparation and characterization of noble metal nanoparticles is an interdisciplinary subject and has attracted much attention due to the fundamental and applied scientific value of nanometer-sized metals.^{15–20} Among these metals, Ag nanoparticles possess unique properties with a wide range of applications, from surface-enhanced Raman spectroscopy^{21,22}

Received: August 15, 2013

Revised: November 17, 2013

Published: December 26, 2013

to their use as an antibacterial agent.^{23–29} Over the past decade, Ag nanocrystals of myriad shapes have been synthesized using various methods.^{18,30–36} In this context, an emerging trend in nanotechnology is the creation of new nanomaterials and the exploration of their novel physical and chemical properties.^{37–39} Often, newly identified nanomaterials bring to light previously undiscovered phenomena. One example, which changed the direction of noble metal research, is the first real-time, *in situ* nucleation and growth of Ag filaments on α -Ag₂WO₄ crystals, driven by an accelerated electron beam from an electronic microscope under high vacuum.⁴⁰

In the present paper, a combined experimental and theoretical study was conducted on the structural arrangement that leads to the interesting growth process of Ag filaments on the α -Ag₂WO₄ crystal surface induced by field-emission scanning electron microscopy (FESEM) and complementary transmission electron microscopy (TEM) with selected-area diffraction (SAD) characterization; the photoluminescence (PL) enhancement of the Ag filaments was also investigated. X-ray diffraction (XRD) with Rietveld refinement, micro-Raman (MR) spectroscopy and Fourier transform infrared spectroscopy (FTIR) were used to analyze the structural order and disorder conditions of the α -Ag₂WO₄ structure prior to the Ag growth. The shape evolution and growth process of the α -Ag₂WO₄ crystals synthesized using a microwave-assisted hydrothermal (MAH) method at different temperatures was analyzed. The first stages of the Ag formation on α -Ag₂WO₄ crystal provoked by electron irradiation were simulated by first-principles calculations based on density functional theory (DFT). The order–disorder structural conditions of the growth evolution and photoluminescence (PL) enhancement were inferred based on the theoretical results.

2. EXPERIMENTAL SECTION

2.1. Synthesis of α -Ag₂WO₄. The typical α -Ag₂WO₄ crystal synthesis procedure was followed: 1×10^{-3} mol sodium tungstate dihydrate (Na₂WO₄·2H₂O, 99.5% purity, Sigma-Aldrich) and 2×10^{-3} mol silver nitrate (AgNO₃, 99.8% purity, Sigma-Aldrich) were separately dissolved in test tubes containing 50 mL deionized water. Before the addition of the salts, 0.5 g sodium dodecyl sulfate (SDS) (C₁₂H₂₅SO₄Na, 99% purity, Sigma-Aldrich) was dissolved in both of the tubes. The 100-mL combined suspension was transferred into a fluorinated ethylene propylene (PTFE) autoclave without stirring. The autoclave was then sealed and placed in a microwave-aided device for hydrothermal synthesis.⁴¹ α -Ag₂WO₄ samples were prepared at different temperatures (100, 120, 140, and 160 °C) for 1 h. The α -Ag₂WO₄ crystals were obtained as light beige, fine powder. The precipitates were collected and washed several times with acetone and dried at room temperature for 6 h.

2.2. Characterizations. The samples were characterized by XRD using a D/Max-2500PC diffractometer (Rigaku, Japan) with Cu K α radiation ($\lambda = 1.5406$ Å) in the 2θ range from 10° to 70° in the normal routine with a scanning velocity of 2°/min and from 10° to 110° with a scanning velocity of 1°/min in the Rietveld routine, both with a step of 0.02°. MR measurements were recorded using a LabRAM HR 800 mm model (Horiba, Jobin-Yvon, France). High-resolution Raman spectra were recorded with a He–Ne laser at 632.81 nm (model CCD DU420AOE325) operating at 25–1000 cm⁻¹ and keeping its maximum output power at 6 mW. A 50- μ m lens was used to prevent sample overheating. FTIR spectra were recorded from 250 to 1000 cm⁻¹ using KBr pellets and a Bomem-Michelson spectrophotometer in transmittance mode (model MB-102). UV–vis spectra were recorded using a Varian spectrophotometer (model Cary 5G) in diffuse reflectance mode. The shapes and sizes of the α -Ag₂WO₄ microcrystals were observed with a field-emission scanning electron microscope (model Inspect F50, FEI Company, Hillsboro, OR) operating at 10

kV. TEM analyses were performed with a CM200-Philips microscope operating at 200 kV. The structural characterization of the samples was estimated using SAD. Specimens for TEM images were obtained by drying droplets of as-prepared samples from an acetone dispersion that had been sonicated for 10 min and deposited on 300-mesh Cu grids. PL measurements were performed with a Monospec 27 monochromator (Thermal Jarrel Ash) coupled to an R446 photomultiplier (Hamamatsu Photonics, Japan). A krypton-ion laser (Coherent Innova 90K; $\lambda = 350.7$ nm) was used as the excitation source; its maximum output power was maintained at 500 mW. The laser beam was passed through an optical chopper, and its maximum power on the sample was maintained at 40 mW. PL measurements were performed at room temperature.

2.3. Theoretical Calculation. Calculations for α -Ag₂WO₄ crystal were performed with a CRYSTAL09 program package.^{42,43} Tungsten was described by a large-core ECP, derived by Hay and Wadt, and modified by Cora et al.⁴⁴ Silver and oxygen centers were described using HAYWSC-311d31G and O (6-31d1G) basis sets, respectively, which were taken from the Crystal Web site.⁴⁵ Becke's three-parameter hybrid nonlocal exchange functional,⁴⁶ was used in combination with a Lee–Yang–Parr gradient-corrected correlation functional (B3LYP).⁴⁷ The diagonalization of the Fock matrix was performed at adequate k -points grids in the reciprocal space. The thresholds controlling the accuracy of the calculation of the Coulomb and exchange integrals were set to 10⁻⁸ (ITOL1 to ITOL4) and 10⁻¹⁴ (ITOL5), and the percent of Fock/Kohn–Sham matrices mixing was set to 40 (IPMIX = 40).⁴² The band structure and the density of states (DOS) projected on atoms and orbitals of bulk α -Ag₂WO₄ were constructed along the appropriate high-symmetry directions of the corresponding irreducible Brillouin zone. To take into account the negative charged system, we inserted two additional electrons in the Ag atom of the [AgO₂] clusters, and in order to simulate properly this electron excess an all-electron basis set (9766-3114d1G),⁴⁵ was used to describe this Ag center.

3. RESULTS AND DISCUSSION

The XRD patterns (Figure 1) indicate that all prepared α -Ag₂WO₄ crystals have an orthorhombic structure without any deleterious phases and belong to the space group $Pn2n$, with a C_{2v} symmetry.⁴⁸ These crystals have sharp and well-defined

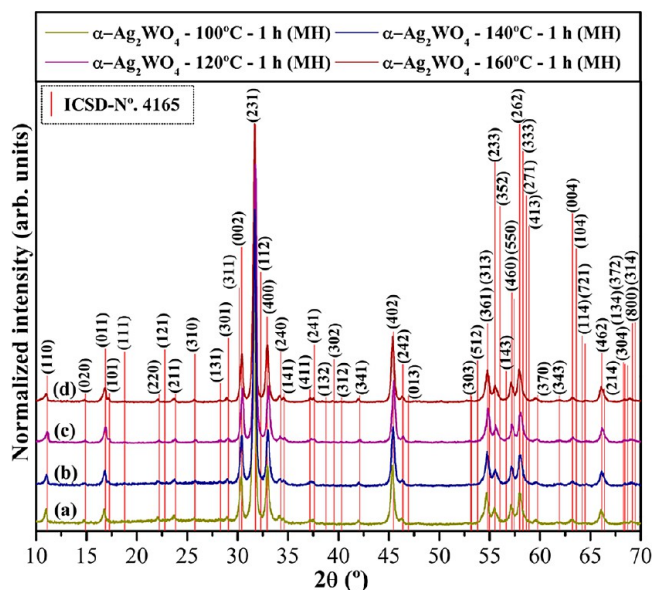


Figure 1. XRD patterns of α -Ag₂WO₄ microcrystals prepared at (a) 100, (b) 120, (c) 140, and (d) 160 °C for 1 h by the MAH method. The vertical lines indicate the position and relative intensity of the data from ICSD No. 4165 for the α -Ag₂WO₄ phase.

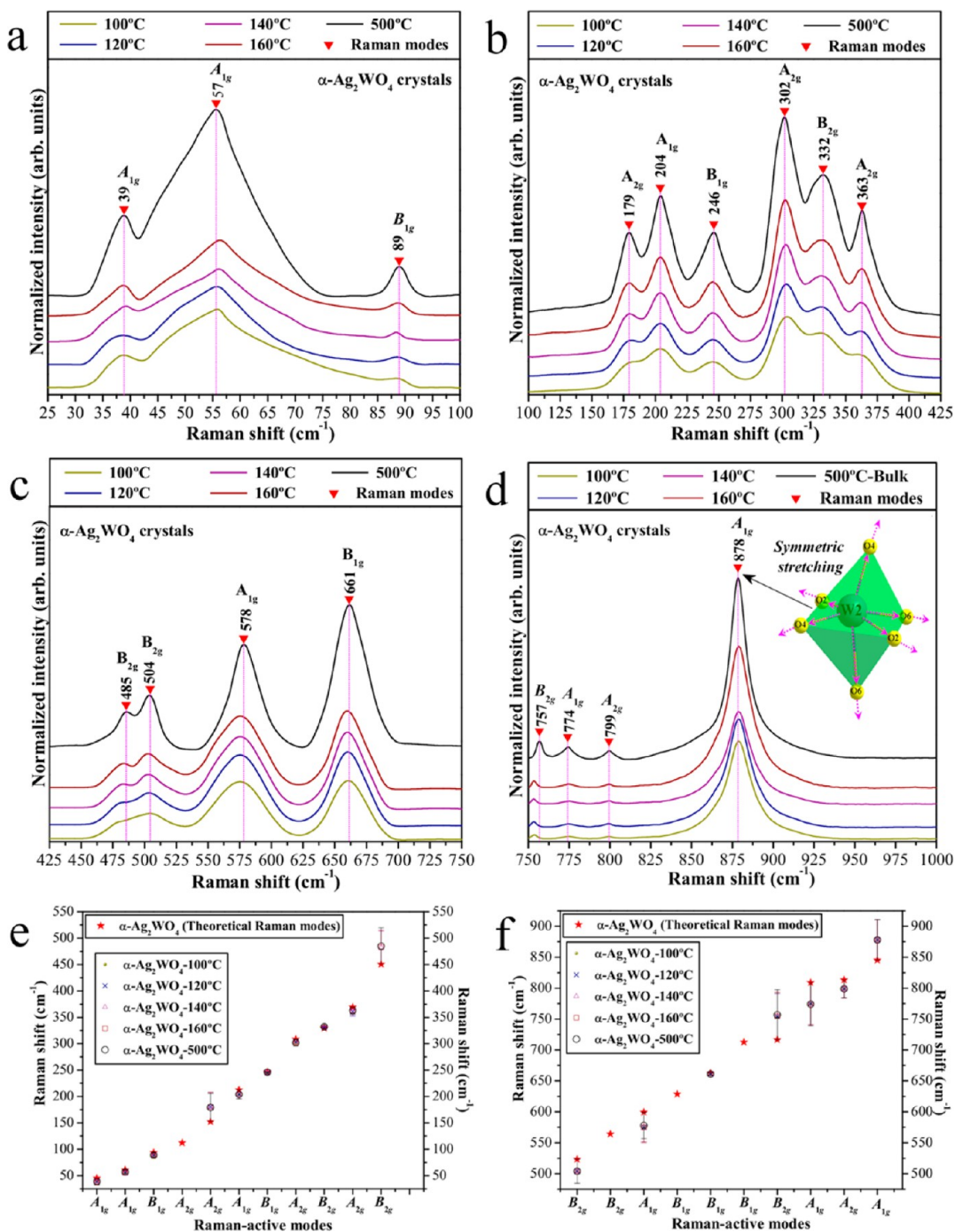


Figure 2. Micro-Raman spectra of $\alpha\text{-Ag}_2\text{WO}_4$ prepared at different temperatures (100, 120, 140, and 160 °C) for 1 h by the MAH method, and by the coprecipitation method heat treated at 500 °C for 1 h (a) from 25 to 100 cm^{-1} , (b) from 100 to 425 cm^{-1} , (c) from 425 to 750 cm^{-1} , and (d) from 750 to 1,000 cm^{-1} . The vertical lines indicate the relative positions of the Raman-active modes. (e, f) Comparison of the theoretical and experimental Raman-active modes from 25 to 550 cm^{-1} and from 500 to 900 cm^{-1} , respectively.

diffraction peaks, which indicate a structural order and crystallinity at long-range. However, it is difficult to confirm the existence of Ag nanoparticles in these crystals based on XRD measurements.⁴⁹ Moreover, all diffraction peaks are in close agreement with the inorganic crystal structure database (ICSD) (N°. 416525) and the literature.⁵⁰ The Rietveld analysis also corroborates these results (Figures S1 and S2 and Tables S1–S5, Supporting Information).

The MR spectra of the $\alpha\text{-Ag}_2\text{WO}_4$ crystals synthesized using the MAH method, and the relative positions of the theoretical

and experimental Raman-active modes are depicted in Figure 2, including labels for the A_{1g} , A_{2g} , B_{1g} , and B_{2g} modes. The active Raman modes can exhibit a variable intensity because the rotation of the x -, y - and z -axes of the $\alpha\text{-Ag}_2\text{WO}_4$ crystals occurs at different scattering of the tensors and components.⁵¹ As can be observed in Figure 2a–d, the MR spectra revealed the presence of 17 Raman-active vibrational modes. Four additional Raman modes (two B_{1g} , one A_{2g} and one B_{2g}) were not detectable experimentally because of their low intensities. Raman spectroscopy can be employed as a probe to investigate

the degree of structural order–disorder at short-range in the materials.^{52,53} Therefore, 17 well-defined Raman-active vibrational modes can be observed for typical α -Ag₂WO₄ crystals, indicating a high degree of short-range structural order in the lattice. However, this behavior was not observed in the α -Ag₂WO₄ crystals synthesized by the MAH method, particularly in the sample treated at 100 °C. It is notable that the MR spectra of the synthesized crystals exhibited broad vibrational modes, indicating structural disorder at short-range. In addition, the disorder increased with the temperature treatment. This characteristic can be related to the very rapid kinetics of the MAH synthetic conditions. The MR spectrum of the sample treated at 100 °C did not present well-defined Raman peaks due to major short-range structural disorder.

Another interesting and important feature is the more pronounced structural local order presented by the lattice in the form of [WO₆] clusters (see Figure 2d), as opposed to the lattice modifier assigned to [AgO_y] ($y = 7, 6, 4$ and 2) clusters (Figure 2a–c). Specifically, the α -Ag₂WO₄ crystals prepared by the MAH method presented more well-defined Raman-active vibrational modes related to the symmetric stretching ($\leftarrow\text{O}\leftarrow\text{W}\rightarrow\text{O}\rightarrow$) bonds of the octahedral [WO₆] clusters than for the external vibrational modes of the distorted [AgO_y] ($y = 7, 6, 4$ and 2) clusters. The theoretical Raman-active modes were calculated through the atomic positions and lattice parameters for the optimized α -Ag₂WO₄ crystals and are illustrated in Figure 2e and f and presented in Table S6. There is good agreement among the Raman-active modes of the α -Ag₂WO₄ crystals obtained in our samples, the first-principles calculation and the previously reported results from Turkovic et al.⁵¹ The two B_{1g}, one A_{2g} and one B_{2g} modes that were not experimentally observed (Figure 2e,f) were predicted by the first-principles calculation, suggesting that their intensity may be too low in the Raman spectrum. The slight variations in the positions of the typical vibrational modes of our sample when compared with those reported in the literature can be attributed to the preparation method, average crystal size, distortions of the (O–Ag–O)/(O–W–O) bonds at short-range and/or intermolecular forces between the [AgO_y]–[WO₆]–[AgO_y] clusters at intermediate range. Moreover, our theoretical calculations do not consider the nonharmonic contribution to the crystal-lattice vibration phonons.

Figure 3 shows the FTIR spectra for the α -Ag₂WO₄ samples and the specific theoretical/experimental infrared modes. Figure 3a indicates that four active IR vibrational modes are possible. According to the literature,⁵⁴ the IR spectrum provides information on the degree of structural order–disorder in the metal–oxygen bonds. Figure 3a–d reveals two intense absorption bands at 830 and 862 cm⁻¹ for all of the α -Ag₂WO₄ microcrystals. These modes are ascribed to the asymmetric stretching vibrations of the ($\leftarrow\text{O}\leftarrow\text{W}\leftarrow\text{O}\leftarrow$)/($\rightarrow\text{O}\rightarrow\text{W}\rightarrow\text{O}\rightarrow$) bonds within the distorted octahedral [WO₆] clusters (see the inset in Figure 3). The active IR vibrational internal mode at 320 cm⁻¹ is related to the symmetric bending vibrations within the distorted [WO₆] clusters,⁵⁵ and the active IR vibrational external mode at 296 cm⁻¹ is assigned to the torsional motion of the distorted octahedral [WO₆] clusters.⁵⁶ Peak positions refer to the IR-active vibrational modes, which are shown in Table S7 and are compared with other methods as reported in the literature.^{55,57} Figure 3b shows the close agreement between the experimental IR-active modes and the theoretically calculated modes, indicated by the ★ symbol. In terms of spectral positions, small deviations in the IR-active

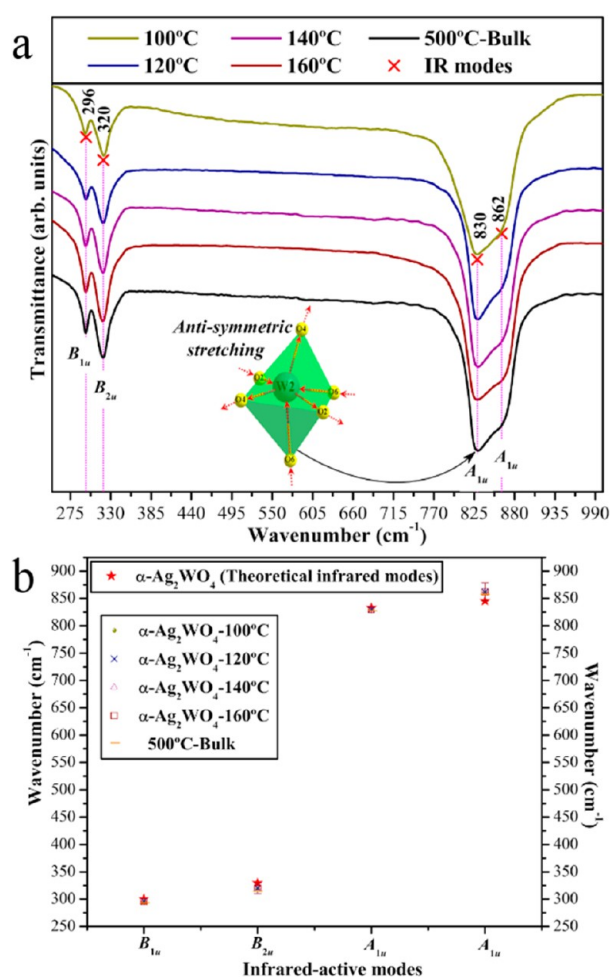


Figure 3. (a) FTIR spectra of α -Ag₂WO₄ prepared at different temperatures (100, 120, 140, and 160 °C) for 1 h by the MAH method. The vertical lines indicate the relative positions of the infrared-active modes. (b) Comparison between the theoretical and experimental infrared-active modes from 250 to 900 cm⁻¹.

modes of the α -Ag₂WO₄ crystals can be attributed to different degrees of interaction and modification of the O–Ag–O and O–W–O bond lengths and/or angles within the [AgO_y] and [WO₆] clusters. The optical band gap energy (E_{gap}) of the α -Ag₂WO₄ crystals was experimentally investigated using the method proposed by Kubelka and Munk.⁵⁸ This methodology is based on the transformation of diffuse reflectance measurements to estimate E_{gap} values with high accuracy within the limits of assumptions when modeled in three dimensions.⁵⁹ According to Tang et al.⁶⁰ and Kim et al.,⁶¹ silver tungstate crystals exhibit an optical absorption spectrum governed by the direct electronic transitions between the valence and conduction bands; this behavior is supported by the theoretical calculations. In this electronic process, after the electronic excitation, the electrons located in the maximum-energy states in the valence band fall back to the minimum-energy states in the conduction band under the same point in the Brillouin zone.

Figure 4a reveals that the band structures for the optimized bulk α -Ag₂WO₄ crystal are characterized by well-defined direct electronic transitions, which is typical of crystalline semiconductor materials. Fundamentally, the top of the VB and the bottom of the CB are in the same Γ to Γ point in the Brillouin zone. The value of the theoretically calculated band gap, 3.55

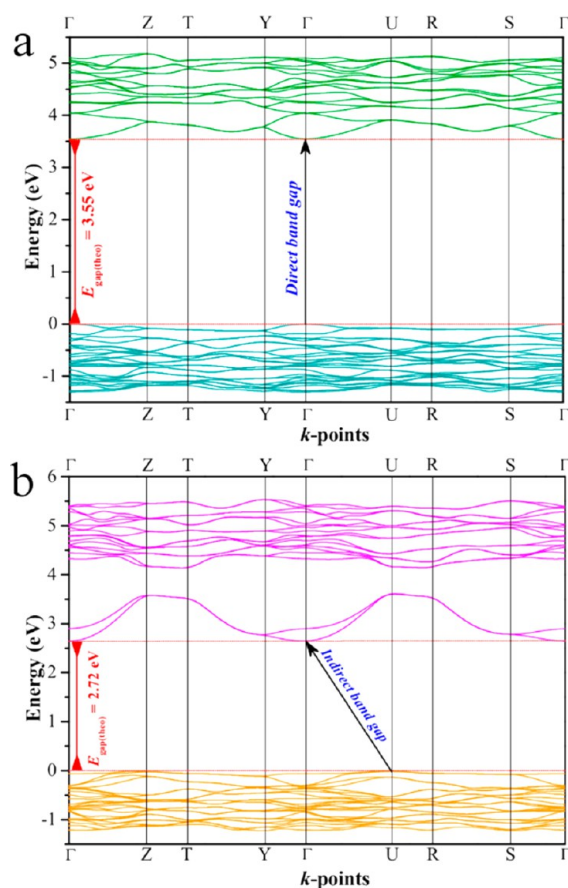


Figure 4. Band structures for optimized bulk α - Ag_2WO_4 crystal (a) in the neutral state and (b) charged with two electrons on the $[\text{AgO}_2]$ clusters.

eV, was slightly higher than the experimental value of ~ 3.2 eV, estimated by UV–vis spectroscopy, for all samples synthesized by the MAH method. This overestimation of the predicted band gap can be due to the fact that it is calculated from the difference between the bottom of the conduction band (CB) and the top of the valence band (VB) within the Kohn–Sham formalism. However, it must be considered that the theoretical calculations estimate the optimized structure with a minimum energy, and the experimental structure derived from the MAH treatment conserves freezing distortions at short and intermediate range, which are not the most stable structures. Moreover, the band structure of this complicated network arrangement of $[\text{WO}_6]$ and $[\text{AgO}_y]$ clusters is basically determined by the W 5d orbitals in the conduction band (CB) and a valence band (VB) derived mostly from hybridized O 2p and Ag 4d orbitals. This reduction in the experimentally optical band gap value is most likely linked to distortions of the $[\text{WO}_6]/[\text{AgO}_y]$ that are favorable to the formation of intermediate energy levels (photogenerated electron–hole pairs) between the VB and CB.

To simulate the electron absorption process based on the α - Ag_2WO_4 structure, theoretical calculations were performed while taking into account the incorporation of two electrons in the structure. An analysis of the α - Ag_2WO_4 structure shows that the $[\text{AgO}_2]$ cluster presents the largest value of positive Mülliken charge for the Ag moiety, with only two adjacent oxygen anions. Therefore, this cluster was the most appropriate candidate to receive the external electron beam irradiation; in a

sense, we inserted two additional electrons in the Ag atom of the $[\text{AgO}_2]$ cluster as a starting point and atomic positions were optimized. The resulting geometry is presented in Table S5b. Figure 4b depicts the band structure for optimized neutral bulk α - Ag_2WO_4 crystal charged with two electrons on the $[\text{AgO}_2]$ clusters. An analysis of the band structure and the DOS (Figure S3a) for the charged system points out that intermediate levels are formed in the vicinity of the CB, which are composed of 5s orbitals of $[\text{AgO}_2]$. Therefore, new energy levels are created in the forbidden region of the band gap, leading to a disordered structure (Figure S3b). The Fermi level is now located at approximately 3.0 eV, considering the VB maximum at the zero-energy level, and the presence of these electron traps reduces the band gap energy to 2.72 eV, becoming indirect from the U point to the Γ point (Figure 4b, Figure S3).

Figure 5 shows the DOS projected on the 4d, 5d, and 2p orbitals of Ag, W and O atoms, respectively, for neutral α - Ag_2WO_4 . The DOS structure of this complex network arrangement can be analyzed in terms of orbitals contribution of the atoms that form $[\text{WO}_6]$ and $[\text{AgO}_y]$ ($y = 7, 6, 4$ and 2) polyhedra. Figure 5a and b show that the projected DOS on the orbitals of the Ag1 and Ag2 atoms, coordinated by seven oxygens ($[\text{AgO}_7]$), are basically derived from the $4d_{xz}$ orbital of the valence band. The same relationship occurs with the Ag3 atom, coordinated by six oxygens ($[\text{AgO}_6]$), as depicted in Figure 5c. When the coordination changes to four ($[\text{AgO}_4]$), as in the Ag4 and Ag5 atoms, the major contribution is derived from the $4d_{xz}$ and $4d_z^2$ orbitals (see Figure 5d,e). Finally, in the bicoordinated Ag6 atom ($[\text{AgO}_2]$) the VB is mostly composed by $4d_{xz}$ orbital (see Figure 5f). The projected DOS on the W atom is basically determined by the 5d orbitals in the conduction band (CB) with more important role of $5d_z^2$ orbitals (Figure 5g). The valence band (VB) is primarily derived from hybridized O 2p (Figure 5h) and Ag 4d orbitals.

A study of the growth of Ag on the α - Ag_2WO_4 surface as a function of exposure time to a scanning electron microscope under an accelerating voltage of 10 kV was carried out. The onset of Ag nanoparticle nuclei on the surface of the α - Ag_2WO_4 crystals was observed by the FESEM images (Figure 6) as soon as the samples began to be analyzed. This behavior was observed for all the samples synthesized at different temperatures, namely, 100, 120, 140, and 160 °C (Figure 6, parts a, c, e and g, respectively). After 5 min of irradiation, the growth of the initial particles of Ag and the onset of new nuclei growth were observed in all the samples (100, 120, 140, and 160 °C) (Figure 6, parts b, d, f, and h, respectively). It is important to emphasize that the sample prepared at 160 °C (Figure 6h) has a higher number of Ag nuclei as well as a higher absorption of existing particles. This behavior was also demonstrated in our previous work.⁴⁰ In this way, the most organized sample (160 °C) favors the nucleation of metallic Ag nanorods. However, the growth process occurs preferentially in samples where the nucleation is smaller. Table S9 (of the Supporting Information) presents the calculated values of the surface energy for (001), (100), (010), (011), (101) and (110) facets of α - Ag_2WO_4 . The surface (100) is the most stable facet, with the higher percentage of the relaxing process. If charged α - Ag_2WO_4 structure is focused on the plane (100) compared to the equilibrium geometry, it can be see an approaching of Ag4 and Ag5 centers (from 4.0 to 3.26 Å) when the system is charged in the vicinity of Ag6 atoms. In addition, Ag6–O distance increases from 2.34 to 2.54 Å showing that this situation favors an accumulation of Ag atoms along the most stable (100)

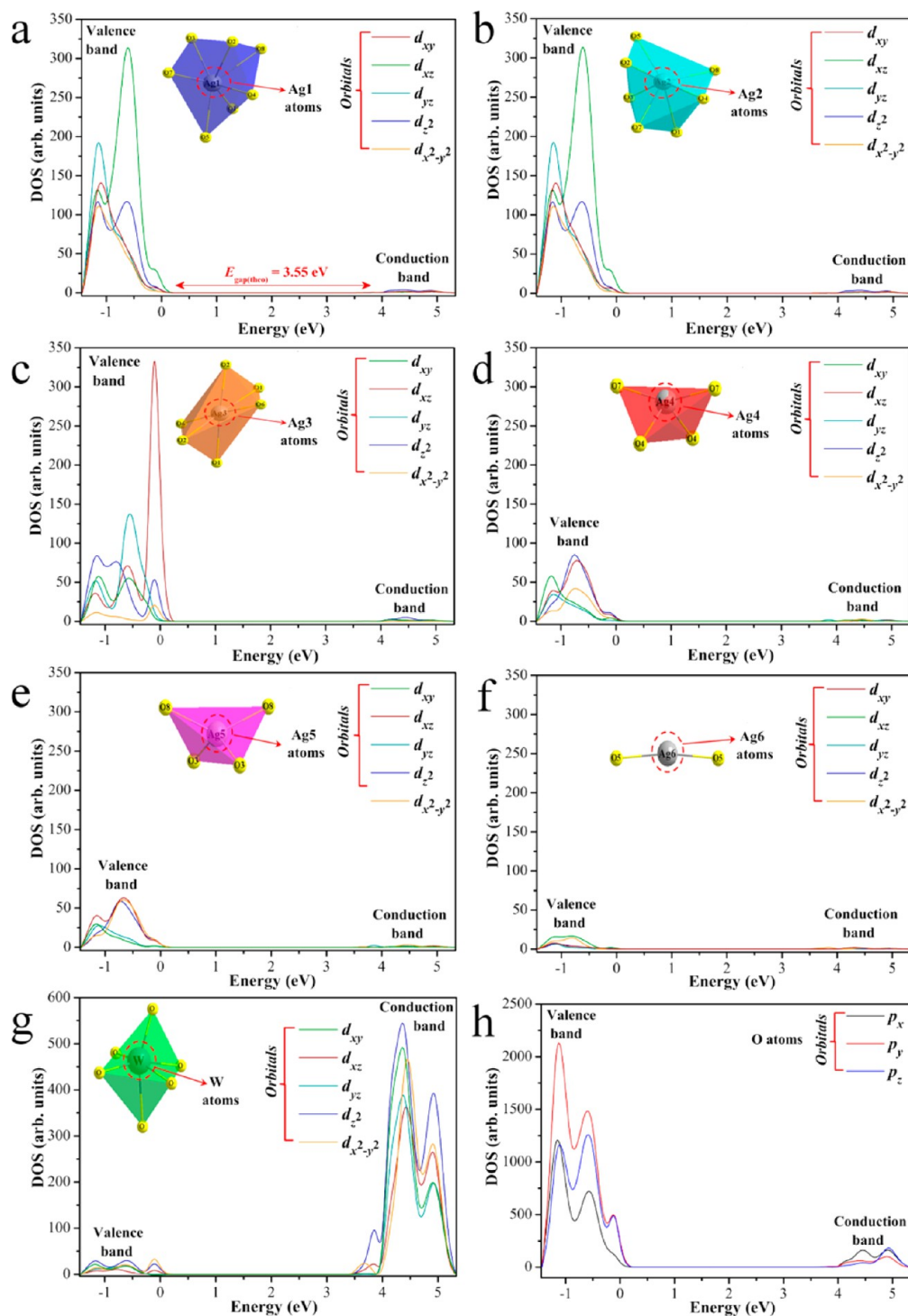


Figure 5. DOS projected on the 4d, 5d, and 2p orbitals of (a–f) Ag, (g) W, and (h) O atoms, respectively.

surface. Therefore, the *ab initio* calculations indicate that the absorption of electrons leads to the disordered structure that facilitates Ag nucleation. It is possible that a more ordered structure has a more homogeneous surface and thus facilitates a more homogeneous nucleation; a more detailed study of this system is necessary to test this possibility. The TEM images of all samples and the structural electron diffraction (SAD) details of the growth process of Ag on the α - Ag_2WO_4 crystals are shown in Figures S4 and S5 and Table S8 in the Supporting Information.

Figure 7 shows the PL spectra recorded at room temperature for the α - Ag_2WO_4 samples, excited by a 350.7 nm line of a krypton ion laser, before and after irradiation by an accelerated electron beam. The PL spectral profiles show typical behavior for multiphonon or multilevel processes, i.e., a solid system where relaxation occurs by several pathways, which involve the participation of numerous energy states within the band gap.⁶² It is generally assumed that the blue-green emission of tungstate is due to the charge-transfer transitions within the $[\text{WO}_4]^{2-}$ complex in ordered systems,^{63–67} or complex cluster vacancies in the former,^{68–70} and/or modified lattice.⁷⁰ It is

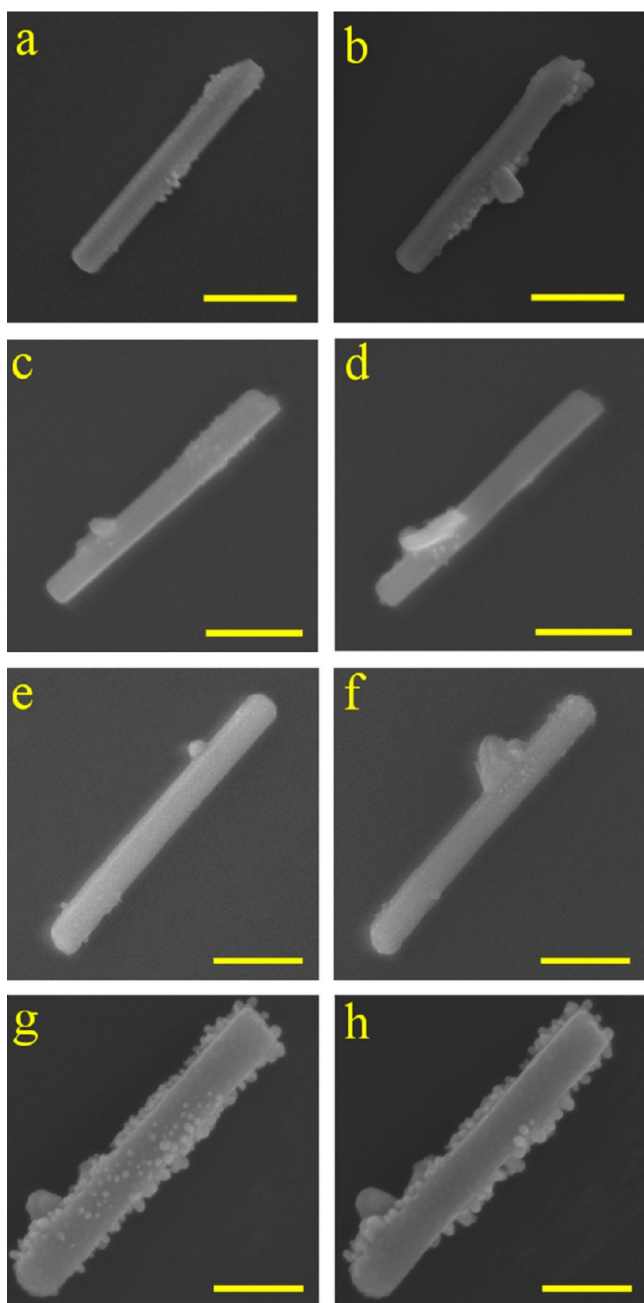


Figure 6. Initial FESEM images of the $\alpha\text{-Ag}_2\text{WO}_4$ samples obtained by the MAH method at (a) 100, (c) 120, (e) 140 and (g) 160 °C. After 5 min, microscopy analyses of the same samples were recorded: (b) 100, (d) 120, (f) 140, and (h) 160 °C. (Scale bar = 400 nm in parts a–f and 200 nm in parts g and h.)

well-known that the physical and chemical properties of materials are strongly correlated with structural factors, primarily the structural order–disorder in the lattice. The materials can be described in terms of the packing of the constituent clusters, which can be considered as the structural motifs. A specific feature of tungstates with a scheelite structure is the existence of $[\text{WO}_6]$ and $[\text{AgO}_y]$ clusters in a crystal lattice.⁷¹ This orthorhombic structure can also be understood in terms of a network of $[\text{WO}_6]$ clusters, linked by strong bonds [...W–O–W...] between the neighboring clusters, whose internal vibration spectra provide information on the structure and order–disorder effects in the crystal lattices.^{72,73} Breaking

the symmetry of these clusters through distortions, breathings and tilts creates a large number of different structures with different material properties; this phenomenon can be related to local (short), intermediate and long-range structural order–disorder. Therefore, for $\alpha\text{-Ag}_2\text{WO}_4$, the material properties can be primarily associated with the constituent clusters, and the disparity or mismatch of both clusters can induce structural order–disorder effects, which significantly influence the luminescence properties of the tungstates.^{74–76}

Disorder in materials can be manifested in many ways; examples include vibrational, spin and orientation disorder (referenced to a periodic lattice) and topological disorder. Topological disorder is the type of disorder associated with glassy and amorphous solid structures in which the structure cannot be defined in terms of a periodic lattice. PL is a powerful probe of certain aspects of short-range (2–5 Å) and medium-range order (5–20 Å), such as clusters where the degree of local order is such that structurally inequivalent sites can be distinguished due to their different types of electronic transitions which are linked to a specific structural arrangement.⁶²

In Figure 7a, the maximum blue PL emission peak is centered at 449 nm for all the samples; however, another diffuse emission in the red region peaking from 621 to 640 nm was also observed. The nucleation–dissolution–recrystallization mechanism favored by the MAH process can be seen as an order–disorder–order process of nature and gives rise to a nonclassical crystallization process.⁷⁷ Using density functional calculations, Ghazi et al.⁷⁸ noted that growth is an order–disorder–order pattern of cyclic nature. Between two ordered clusters, growth proceeds via disordered clusters, and global order emerges suddenly with the addition of only one or two atoms. In this sense, the different intensities in the emission profiles can be attributed to slight differences in the defect densities linked to the distorted clusters and complex vacancies generated by the MAH heat treatment. The first emission peak can be related to distorted $[\text{WO}_6]$ octahedra that are, in the case of our samples, more ordered, in accordance with the MR and IR spectral data and previous reports.^{63–67} The emission in the red spectrum region is most likely linked to the $[\text{AgO}_y]$ clusters that form complex vacancies, inducing more disorder and deeper defects in the forbidden band gap. However, other factors may also be involved, such as the degree of aggregation and the orientation between particles, the variations in the particle size distribution, the morphology of the particles and surface defects. All these factors have an influence on the intensity of the PL emission.

The PL profile of irradiated $\alpha\text{-Ag}_2\text{WO}_4$ depicted in Figure 7b is quite different from the nonirradiated PL profile (Figure 7a). No blue shift is observed in the emission maximum, indicating that the $[\text{WO}_6]$ clusters are unchanged by the irradiation (Figure 7c,f). However, the profile of the PL emission in the red region of the spectra is changed. As discussed above, these changes can be attributed to the $[\text{AgO}_y]$ clusters becoming more disordered by the Ag metallic growth on the surface. This process generates complex vacancies of V_{Ag}' and V_{O}^{\times} (where $V_{\text{O}}^{\times} = V_{\text{O}}^{\bullet}, V_{\text{O}}^{\bullet\bullet}$), but it is clear that the $[\text{WO}_6]$ surface clusters should also be slightly disordered as a result of Ag migration and Ag nanorod formation. As predicted by first-principles calculations, in the disordered structure the electronic levels are significantly affected by the inclusion of electrons, as it is observed in the band gap structure, favoring the red emission. The samples prepared at 100 (Figure 7c), 120 (Figure 7d), and

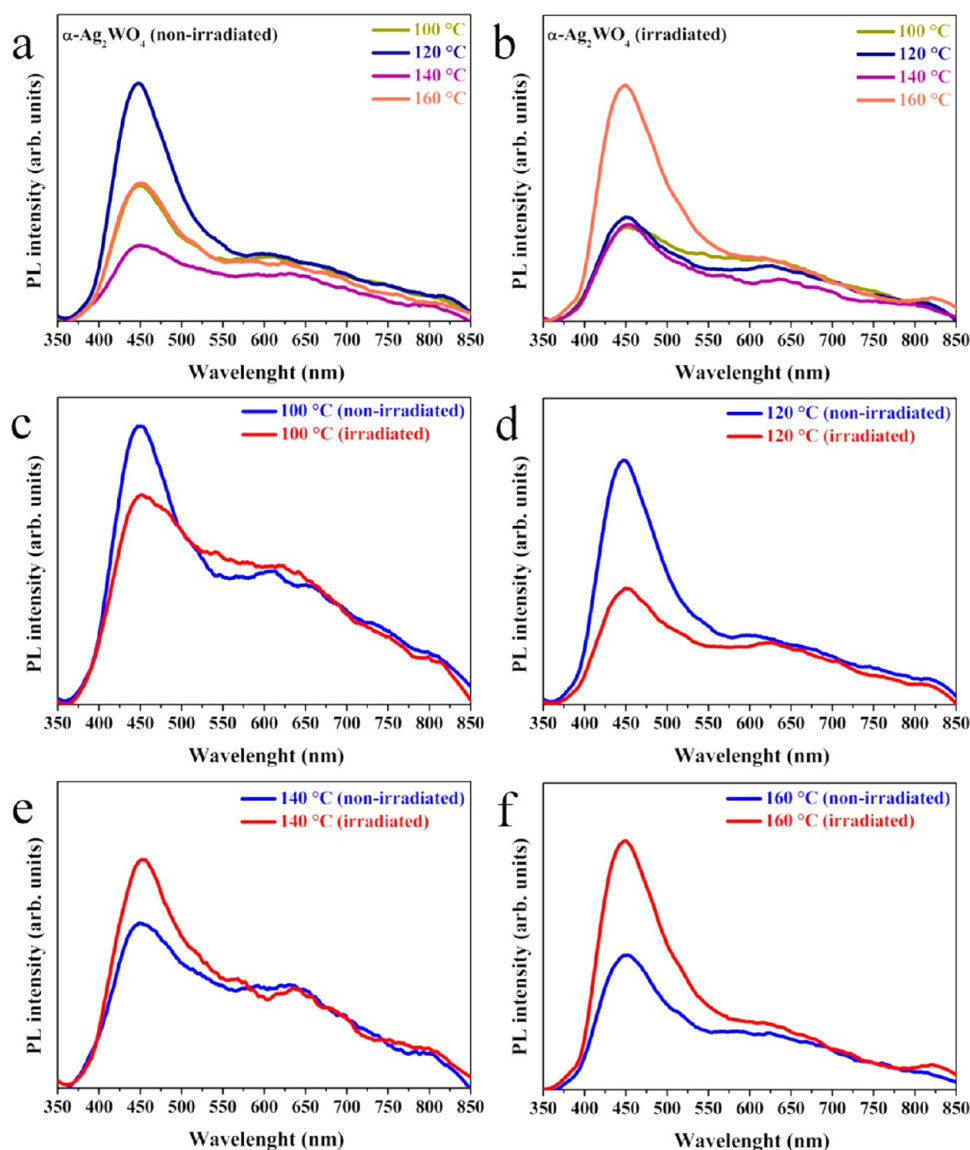


Figure 7. PL spectra recorded at room temperature of the α - Ag_2WO_4 crystals obtained by the MAH method at 100, 120, 140, and 160 °C, excited by a 350.7 nm line of a krypton ion laser (a) before and (b) after irradiation by an accelerated electron beam. For better visualization, we show the spectrum of each individual sample: (c) 100, (d) 120, (e) 140, and (f) 160 °C irradiated (red) and nonirradiated (blue).

140 °C (Figure 7e) show intermediate PL intensities. The maximum enhancement in PL emission after irradiation was observed in the sample heat-treated at 160 °C (Figure 7f). This sample presents the highest degree of structural order prior to irradiation, as discussed in the MR and FTIR analysis, and the highest nucleation rate after irradiation, as observed by FESEM (Figure 6h). The more abundant and homogeneous nucleation favored by the more ordered structure results in more V'_{Ag} and V''_{O} complex vacancies and a larger effect on the PL enhancement.

4. CONCLUSIONS

In this study, α - Ag_2WO_4 particles were successfully synthesized by an MAH method; XRD patterns and Rietveld analysis confirmed the orthorhombic structure obtained. The physical/chemical properties and the corresponding performance of the α - Ag_2WO_4 crystals are closely related to the crystal structure, and in the present case, the local electric fields or polarized fields in the distorted metal–oxygen polyhedra, namely $[\text{WO}_6]$

and $[\text{AgO}_y]$ ($y = 7, 6, 4,$ and 2). MR and FTIR spectroscopy indicate that the MAH method employed in the synthesis of α - Ag_2WO_4 crystals leads to the freezing of distorted $[\text{WO}_6]$ and $[\text{AgO}_y]$ clusters. An external electron beam irradiation induces the formation and crystal growth of Ag filaments on the α - Ag_2WO_4 crystal and a PL enhancement. This finding is reshaping our understanding of these molecular processes, revealing previously hidden subtleties. A theoretical investigation using density functional theory (DFT) was carried out to understand the introduction of electrons into the α - Ag_2WO_4 lattice. The results indicate that the electron-induced growth process of Ag on α - Ag_2WO_4 crystal is closely connected with the structural and electronic properties of the $[\text{AgO}_2]$ cluster; this process results in a drastic increase of the structural and electronic disorder, as evidenced by the decrease in the band gap from 3.55 to 2.72 eV. Finally, no blue shift of the emission maximum was observed, indicating that the $[\text{WO}_6]$ clusters were unchanged by the irradiation; however, changes were observed in the red region of the PL profile. These changes

were attributed to unstable $[\text{AgO}_y]$ clusters that became disordered by the growth of metallic Ag on the surface, leading to complex vacancies. First-principles calculations predicted that this process would lead to a disordered structure with deep defects inserted in the band gap, favoring the red emission. The results of this research provide fundamental insight into the PL properties of $\alpha\text{-Ag}_2\text{WO}_4$ crystals, the electron-induced synthesis of Ag/ $\alpha\text{-Ag}_2\text{WO}_4$ and its relationship with the morphology by controlling surface/bulk defects. We believe that this process may also be applicable for controlling other properties such as microbial activity and photodegradation.

■ ASSOCIATED CONTENT

■ Supporting Information

Figures and tables of Rietveld refinement analyses of the $\alpha\text{-Ag}_2\text{WO}_4$ crystal, DFT analysis, and TEM analysis with the corresponding SAD characterization. This material is available free of charge via the Internet at <http://pubs.acs.org>.

■ AUTHOR INFORMATION

Corresponding Author

*E-mail: (D.P.V.) volanti@ibilce.unesp.br.

Notes

The authors declare no competing financial interest.

■ ACKNOWLEDGMENTS

This work is financially supported by the National Council for Scientific and Technological Development (CNPq), São Paulo Research Foundation (FAPESP), Prometeo/2009/053 (Generalitat Valenciana) and Ministerio de Economía y Competitividad (Spain), CTQ2012-36253-C03-02, and the Spanish–Brazilian program (PHB2009-0065-PC) for their financial support. TEM facilities were provided by LME-IQ-UNESP.

■ REFERENCES

- (1) Kamino, T.; Sasaki, K.; Saka, H. High Resolution Electron Microscopy in Situ Observation of Dynamic Behavior of Grain Boundaries and Interfaces at Very High Temperatures. *Microsc. Microanal.* **1997**, *3*, 393–408.
- (2) Saka, H.; Kamino, T.; Arai, S.; Sasaki, K. In Situ Heating Transmission Electron Microscopy. *MRS Bull.* **2008**, *33*, 93–100.
- (3) Yaguchi, T.; Kanemura, T.; Shimizu, T.; Imamura, D.; Watabe, A.; Kamino, T. Development of a Technique for in Situ High Temperature TEM Observation of Catalysts in a Highly Moisturized Air Atmosphere. *J. Electron Microsc.* **2012**, *61*, 199–206.
- (4) Parent, L. R.; Robinson, D. B.; Woehl, T. J.; Ristenpart, W. D.; Evans, J. E.; Browning, N. D.; Arslan, I. Direct in Situ Observation of Nanoparticle Synthesis in a Liquid Crystal Surfactant Template. *ACS Nano* **2012**, *6*, 3589–3596.
- (5) Nam, S.-W.; Chung, H.-S.; Lo, Y. C.; Qi, L.; Li, J.; Lu, Y.; Johnson, A. T. C.; Jung, Y.; Nukala, P.; Agarwal, R. Electrical Wind Force-Driven and Dislocation-Templated Amorphization in Phase-Change Nanowires. *Science* **2012**, *336*, 1561–1566.
- (6) Xin, H. L.; Zheng, H. In Situ Observation of Oscillatory Growth of Bismuth Nanoparticles. *Nano Lett.* **2012**, *12*, 1470–1474.
- (7) Dayeh, S. A.; Picraux, S. T. Direct Observation of Nanoscale Size Effects in Ge Semiconductor Nanowire Growth. *Nano Lett.* **2010**, *10*, 4032–4039.
- (8) Mandl, B.; Stangl, J.; Hilner, E.; Zakharov, A. A.; Hillerich, K.; Dey, A. W.; Samuelson, L.; Bauer, G.; Deppert, K.; Mikkelsen, A. Growth Mechanism of Self-Catalyzed Group III-V Nanowires. *Nano Lett.* **2010**, *10*, 4443–4449.
- (9) Sohn, J. I.; Joo, H. J.; Porter, A. E.; Choi, C.-J.; Kim, K.; Kang, D. J.; Welland, M. E. Direct Observation of the Structural Component of

the Metal-Insulator Phase Transition and Growth Habits of Epitaxially Grown VO_2 Nanowires. *Nano Lett.* **2007**, *7*, 1570–1574.

(10) Radisic, A.; Ross, F. M.; Searson, P. C. In Situ Study of the Growth Kinetics of Individual Island Electrodeposition of Copper. *J. Phys. Chem. B* **2006**, *110*, 7862–7868.

(11) Williamson, M. J.; Tromp, R. M.; Vereecken, P. M.; Hull, R.; Ross, F. M. Dynamic Microscopy of Nanoscale Cluster Growth at the Solid-Liquid Interface. *Nat. Mater.* **2003**, *2*, 532–536.

(12) Evans, J. E.; Jungjohann, K. L.; Browning, N. D.; Arslan, I. Controlled Growth of Nanoparticles from Solution with in Situ Liquid Transmission Electron Microscopy. *Nano Lett.* **2011**, *11*, 2809–2813.

(13) Yuk, J. M.; Park, J.; Ercius, P.; Kim, K.; Hellebusch, D. J.; Crommie, M. F.; Lee, J. Y.; Zettl, A.; Alivisatos, A. P. High-Resolution Em of Colloidal Nanocrystal Growth Using Graphene Liquid Cells. *Science* **2012**, *336*, 61–64.

(14) Park, J.; Zheng, H. M.; Lee, W. C.; Geissler, P. L.; Rabani, E.; Alivisatos, A. P. Direct Observation of Nanoparticle Superlattice Formation by Using Liquid Cell Transmission Electron Microscopy. *ACS Nano* **2012**, *6*, 2078–2085.

(15) Burda, C.; Chen, X. B.; Narayanan, R.; El-Sayed, M. A. Chemistry and Properties of Nanocrystals of Different Shapes. *Chem. Rev.* **2005**, *105*, 1025–1102.

(16) Xia, Y.; Xiong, Y.; Lim, B.; Skrabalak, S. A. Shape-Controlled Synthesis of Metal Nanocrystals: Simple Chemistry Meets Complex Physics? *Angew. Chem., Int. Ed.* **2009**, *48*, 60–103.

(17) Murphy, C. J.; Gole, A. M.; Stone, J. W.; Sisco, P. N.; Alkilany, A. M.; Goldsmith, E. C.; Baxter, S. C. Gold Nanoparticles in Biology: Beyond Toxicity to Cellular Imaging. *Acc. Chem. Res.* **2008**, *41*, 1721–1730.

(18) Rycenga, M.; Cobley, C. M.; Zeng, J.; Li, W. Y.; Moran, C. H.; Zhang, Q.; Qin, D.; Xia, Y. N. Controlling the Synthesis and Assembly of Silver Nanostructures for Plasmonic Applications. *Chem. Rev.* **2011**, *111*, 3669–3712.

(19) Lim, B.; Jiang, M.; Camargo, P. H. C.; Cho, E. C.; Tao, J.; Lu, X.; Zhu, Y.; Xia, Y. Pd-Pt Bimetallic Nanodendrites with High Activity for Oxygen Reduction. *Science* **2009**, *324*, 1302–1305.

(20) Anker, J. N.; Hall, W. P.; Lyandres, O.; Shah, N. C.; Zhao, J.; Van Duyne, R. P. Biosensing with Plasmonic Nanosensors. *Nat. Mater.* **2008**, *7*, 442–453.

(21) Hutter, E.; Fendler, J. H. Exploitation of Localized Surface Plasmon Resonance. *Adv. Mater.* **2004**, *16*, 1685–1706.

(22) Hao, E.; Schatz, G. C. Electromagnetic Fields around Silver Nanoparticles and Dimers. *J. Chem. Phys.* **2004**, *120*, 357–366.

(23) Liu, J.; Sonshine, D. A.; Shervani, S.; Hurt, R. H. Controlled Release of Biologically Active Silver from Nanosilver Surfaces. *ACS Nano* **2010**, *4*, 6903–6913.

(24) Gunawan, C.; Teoh, W. Y.; Marquis, C. P.; Liffa, J.; Amal, R. Reversible Antimicrobial Photoswitching in Nanosilver. *Small* **2009**, *5*, 341–344.

(25) Kittler, S.; Greulich, C.; Diendorf, J.; Koeller, M.; Epple, M. Toxicity of Silver Nanoparticles Increases During Storage Because of Slow Dissolution under Release of Silver Ions. *Chem. Mater.* **2010**, *22*, 4548–4554.

(26) Sotiropoulos, G. A.; Teleki, A.; Camenzind, A.; Krumeich, F.; Meyer, A.; Panke, S.; Pratsinis, S. E. Nanosilver on Nanostructured Silica: Antibacterial Activity and Ag Surface Area. *Chem. Eng. J.* **2011**, *170*, 547–554.

(27) Christopher, P.; Xin, H.; Linic, S. Visible-Light-Enhanced Catalytic Oxidation Reactions on Plasmonic Silver Nanostructures. *Nat. Chem.* **2011**, *3*, 467–472.

(28) Kumar, A.; Vemula, P. K.; Ajayan, P. M.; John, G. Silver-Nanoparticle-Embedded Antimicrobial Paints Based on Vegetable Oil. *Nat. Mater.* **2008**, *7*, 236–241.

(29) Chernousova, S.; Epple, M. Silver as Antibacterial Agent: Ion, Nanoparticle, and Metal. *Angew. Chem., Int. Ed.* **2013**, *52*, 1636–1653.

(30) Jin, R. C.; Cao, Y. W.; Mirkin, C. A.; Kelly, K. L.; Schatz, G. C.; Zheng, J. G. Photoinduced Conversion of Silver Nanospheres to Nanoprisms. *Science* **2001**, *294*, 1901–1903.

- (31) Jana, N. R.; Gearheart, L.; Murphy, C. J. Wet Chemical Synthesis of Silver Nanorods and Nanowires of Controllable Aspect Ratio. *Chem. Commun.* **2001**, 617–618.
- (32) Tao, A.; Sinsersuksakul, P.; Yang, P. Polyhedral Silver Nanocrystals with Distinct Scattering Signatures. *Angew. Chem., Int. Ed.* **2006**, *45*, 4597–4601.
- (33) Pietrobon, B.; Kitaev, V. Photochemical Synthesis of Monodisperse Size-Controlled Silver Decahedral Nanoparticles and Their Remarkable Optical Properties. *Chem. Mater.* **2008**, *20*, 5186–5190.
- (34) Zhang, J.; Li, S.; Wu, J.; Schatz, G. C.; Mirkin, C. A. Plasmon-Mediated Synthesis of Silver Triangular Bipyramids. *Angew. Chem., Int. Ed.* **2009**, *48*, 7787–7791.
- (35) Coskun, S.; Aksoy, B.; Unalan, H. E. Polyol Synthesis of Silver Nanowires: An Extensive Parametric Study. *Cryst. Growth Des.* **2011**, *11*, 4963–4969.
- (36) Lee, J.; Lee, P.; Lee, H.; Lee, D.; Lee, S. S.; Ko, S. H. Very Long Ag Nanowire Synthesis and Its Application in a Highly Transparent, Conductive and Flexible Metal Electrode Touch Panel. *Nanoscale* **2012**, *4*, 6408–6414.
- (37) Ariga, K.; Vinu, A.; Yamauchi, Y.; Ji, Q. M.; Hill, J. P. Nanoarchitectonics for Mesoporous Materials. *Bull. Chem. Soc. Jpn.* **2012**, *85*, 1–32.
- (38) Xiang, Q.; Yu, J.; Jaroniec, M. Graphene-Based Semiconductor Photocatalysts. *Chem. Soc. Rev.* **2012**, *41*, 782–796.
- (39) Saha, K.; Agasti, S. S.; Kim, C.; Li, X.; Rotello, V. M. Gold Nanoparticles in Chemical and Biological Sensing. *Chem. Rev.* **2012**, *112*, 2739–2779.
- (40) Longo, E.; Cavalcante, L. S.; Volanti, D. P.; Gouveia, A. F.; Longo, V. M.; Varela, J. A.; Orlandi, M. O.; Andres, J. Direct in Situ Observation of the Electron-Driven Synthesis of Ag Filaments on α - Ag_2WO_4 Crystals. *Sci. Rep.* **2013**, *3*.
- (41) Longo da Silva, E.; Arana Varela, J.; de Araujo Almeida, D. K.; Paschoalini Volanti, D. Microwave Aided Device for Hydrothermal Synthesis of Nanostructured Oxides, Particularly Obtaining Particles of Metal Oxides, Comprises Container, in which Hydrothermal Reaction Takes Place, and Lid for Container. BR200815393-A2, 07 Dec 2010.
- (42) Dovesi, R.; Saunders, V. R. R. C.; Orlando, R.; Zicovich-Wilson, C. M.; Pascale, F.; Civalieri, B.; Doll, K.; Harrison, N. M.; Bush, I. J.; D'Arco, P.; Llunell, M., *Crystal09 User's Manual*. University of Torino: Torino, Italy, 2009.
- (43) Dovesi, R.; Orlando, R.; Civalieri, B.; Roetti, C.; Saunders, V. R.; Zicovich-Wilson, C. M. Crystal: A Computational Tool for the Ab Initio Study of the Electronic Properties of Crystals. *Z. Kristallogr.* **2005**, *220*, 571–573.
- (44) Cora, F.; Patel, A.; Harrison, N. M.; Dovesi, R.; Catlow, C. R. A. An Ab Initio Hartree-Fock Study of the Cubic and Tetragonal Phases of Bulk Tungsten Trioxide. *J. Am. Chem. Soc.* **1996**, *118*, 12174–12182.
- (45) Pileni, M. P. Supracrystals of Inorganic Nanocrystals: An Open Challenge for New Physical Properties. *Acc. Chem. Res.* **2008**, *41*, 1799–1809.
- (46) Becke, A. D. Density-Functional Thermochemistry. 3. The Role of Exact Exchange. *J. Chem. Phys.* **1993**, *98*, 5648–5652.
- (47) Lee, C. T.; Yang, W. T.; Parr, R. G. Development of the Colle-Salvetti Correlation-Energy Formula into a Functional of the Electron-Density. *Phys. Rev. B* **1988**, *37*, 785–789.
- (48) Skarstad, P. M.; Geller, S. $(\text{W}_4\text{O}_{16})_8^-$ Polyion in High-Temperature Modification of Silver Tungstate. *Mater. Res. Bull.* **1975**, *10*, 791–799.
- (49) Wang, P.; Huang, B.; Qin, X.; Zhang, X.; Dai, Y.; Whangbo, M.-H. Ag/AgBr/ WO_3 Center Dot H_2O : Visible-Light Photocatalyst for Bacteria Destruction. *Inorg. Chem.* **2009**, *48*, 10697–10702.
- (50) Stone, D.; Liu, J.; Singh, D. P.; Muratore, C.; Voevodin, A. A.; Mishra, S.; Rebholz, C.; Ge, Q.; Aouadi, S. M. Layered Atomic Structures of Double Oxides for Low Shear Strength at High Temperatures. *Scr. Mater.* **2010**, *62*, 735–738.
- (51) Turkovic, A.; Fox, D. L.; Scott, J. F.; Geller, S.; Ruse, G. F. High-Temperature Raman-Spectroscopy of Silver Tetra-Tungstate, $\text{Ag}_8\text{W}_4\text{O}_{16}$. *Mater. Res. Bull.* **1977**, *12*, 189–195.
- (52) Marques, A. P. A.; Motta, F. V.; Leite, E. R.; Pizani, P. S.; Varela, J. A.; Longo, E.; de Melo, D. M. A. Evolution of Photoluminescence as a Function of the Structural Order or Disorder in CaMoO_4 Nanopowders. *J. Appl. Phys.* **2008**, *104*.
- (53) Pereira, P. F. S.; de Moura, A. P.; Nogueira, I. C.; Lima, M. V. S.; Longo, E.; de Sousa Filho, P. C.; Serra, O. A.; Nassar, E. J.; Rosa, I. L. V. Study of the Annealing Temperature Effect on the Structural and Luminescent Properties of SrWO_4 :Eu Phosphors Prepared by a Non-Hydrolytic Sol-Gel Process. *J. Alloys Compd.* **2012**, *526*, 11–21.
- (54) Cavalcante, L. S.; Batista, F. M. C.; Almeida, M. A. P.; Rabelo, A. C.; Nogueira, I. C.; Batista, N. C.; Varela, J. A.; Santos, M. R. M. C.; Longo, E.; Siu Li, M. Structural Refinement, Growth Process, Photoluminescence and Photocatalytic Properties of $(\text{Ba}_{1-x}\text{Pr}_{2x/3})\text{WO}_4$ Crystals Synthesized by the Coprecipitation Method. *RSC Adv.* **2012**, *2*, 6438–6454.
- (55) Clark, G. M.; Doyle, W. P. Infra-Red Spectra of Anhydrous Molybdates and Tungstates. *Spectrochim. Acta* **1966**, *22*, 1441.
- (56) Siritwong, P.; Thongtem, T.; Phuruangrat, A.; Thongtem, S. Hydrothermal Synthesis, Characterization, and Optical Properties of Wolframite ZnWO_4 Nanorods. *CrystEngComm* **2011**, *13*, 1564–1569.
- (57) McKechnie, J. S.; Turner, L. D. S.; Vincent, C. A.; Bonino, F.; Lazzari, M.; Rivolta, B. Silver Monotungstates, Ditungstates and Tetratungstates. *J. Inorg. Nucl. Chem.* **1979**, *41*, 177–179.
- (58) Kubelka, P.; Munk, F. Ein Beitrag Zur Optik Der Farbanstriche. *Z. Tech. Phys.* **1931**, *12*, 593–601.
- (59) Myrick, M. L.; Simcock, M. N.; Baranowski, M.; Brooke, H.; Morgan, S. L.; McCutcheon, J. N. The Kubelka-Munk Diffuse Reflectance Formula Revisited. *Appl. Spectrosc. Rev.* **2011**, *46*, 140–165.
- (60) Tang, J. W.; Ye, J. H. Correlation of Crystal Structures and Electronic Structures and Photocatalytic Properties of the W-Containing Oxides. *J. Mater. Chem.* **2005**, *15*, 4246–4251.
- (61) Kim, D. W.; Cho, I.-S.; Lee, S.; Bae, S.-T.; Shin, S. S.; Han, G. S.; Jung, H. S.; Hong, K. S. Photophysical and Photocatalytic Properties of $\text{Ag}_2\text{M}_2\text{O}_7$ (M = Mo, W). *J. Am. Ceram. Soc.* **2010**, *93*, 3867–3872.
- (62) Longo, V. M.; Cavalcante, L. S.; Paris, E. C.; Sczancoski, J. C.; Pizani, P. S.; Li, M. S.; Andres, J.; Longo, E.; Varela, J. A. Hierarchical Assembly of CaMoO_4 Nano-Octahedrons and Their Photoluminescence Properties. *J. Phys. Chem. C* **2011**, *115*, 5207–5219.
- (63) Yin, Y.; Gao, Y.; Sun, Y.; Zhou, B.; Ma, L.; Wu, X.; Zhang, X. Synthesis and Photoluminescent Properties of CaMoO_4 Nanostructures at Room Temperature. *Mater. Lett.* **2010**, *64*, 602–604.
- (64) Groeninck, J. A.; Hakfoort, C.; Blasse, G. Luminescence of Calcium Molybdate. *Phys Status Solidi A* **1979**, *54*, 329–336.
- (65) Ryu, J. H.; Yoon, J. W.; Lim, C. S.; Oh, W. C.; Shim, K. B. Microwave-Assisted Synthesis of CaMoO_4 Nano-Powders by a Citrate Complex Method and Its Photoluminescence Property. *J. Alloys Compd.* **2005**, *390*, 245–249.
- (66) Campos, A. B.; Simoes, A. Z.; Longo, E.; Varela, J. A.; Longo, V. M.; de Figueiredo, A. T.; de Vicente, F. S.; Hernandez, A. C. Mechanisms Behind Blue, Green, and Red Photoluminescence Emissions in CaWO_4 and CaMoO_4 Powders. *Appl. Phys. Lett.* **2007**, *91*.
- (67) Xu, C.; Zou, D.; Guo, H.; Jie, F.; Ying, T. Luminescence Properties of Hierarchical CaMoO_4 Microspheres Derived by Ionic Liquid-Assisted Process. *J. Lumin.* **2009**, *129*, 474–477.
- (68) Liu, T.; Chen, J.; Yan, F. Optical Polarized Properties Related to the Oxygen Vacancy in the CaMoO_4 Crystal. *J. Lumin.* **2009**, *129*, 101–104.
- (69) Pu, C.; Liu, T.; Zhang, Q. Study of the Electronic Structures of CaMoO_4 Crystal Related to Oxygen Vacancy. *Phys. Status Solidi B* **2008**, *245*, 1586–1589.
- (70) Longo, V. M.; de Figueiredo, A. T.; Campos, A. B.; Espinosa, J. W. M.; Hernandez, A. C.; Taft, C. A.; Sambrano, J. R.; Varela, J. A.; Longo, E. Different Origins of Green-Light Photoluminescence

Emission in Structurally Ordered and Disordered Powders of Calcium Molybdate. *J. Phys. Chem. A* **2008**, *112*, 8920–8928.

(71) Wyckoff, R. W. G., *Crystal Structures*. Wiley: New York, 1948; Vol. II.

(72) Phuruangrat, A.; Thongtem, T.; Thongtem, S. Synthesis of Lead Molybdate and Lead Tungstate Via Microwave Irradiation Method. *J. Cryst. Growth* **2009**, *311*, 4076–4081.

(73) Phuruangrat, A.; Thongtem, T.; Thongtem, S. Barium Molybdate and Barium Tungstate Nanocrystals Synthesized by a Cyclic Microwave Irradiation. *J. Phys. Chem. Solids* **2009**, *70*, 955–959.

(74) Itoh, M.; Fujita, M. Optical Properties of Scheelite and Rospite PbWO₄ Crystals. *Phys. Rev. B* **2000**, *62*, 12825–12830.

(75) Nikl, M.; Bohacek, P.; Mihokova, E.; Kobayashi, M.; Ishii, M.; Usuki, Y.; Babin, V.; Stolovich, A.; Zazubovich, S.; Bacci, M. Excitonic Emission of Scheelite Tungstates AWO₄ (A = Pb, Ca, Ba, Sr). *J. Lumin.* **2000**, *87–9*, 1136–1139.

(76) Gracia, L.; Longo, V. M.; Cavalcante, L. S.; Beltran, A.; Avansi, W.; Li, M. S.; Mastelaro, V. R.; Varela, J. A.; Longo, E.; Andres, J. Presence of Excited Electronic State in CaWO₄ Crystals Provoked by a Tetrahedral Distortion: An Experimental and Theoretical Investigation. *J. Appl. Phys.* **2011**, *110*.

(77) Luo, Z. J.; Li, H. M.; Shu, H. M.; Wang, K.; Xia, J. X.; Yan, Y. S. Synthesis of BaMoO₄ Nestlike Nanostructures under a New Growth Mechanism. *Cryst. Growth Des.* **2008**, *8*, 2275–2281.

(78) Ghazi, S. M.; Zorriasatein, S.; Kanhere, D. G. Building Clusters Atom-by-Atom: From Local Order to Global Order. *J. Phys. Chem. A* **2009**, *113*, 2659–2662.